Chemical Papers (2023) 77:6959–6973
https://doi.org/10.1007/s11696-023-02989-9

ORIGINAL PAPER

Enhancement of the mechanical and antibacterial properties of Bis-GMA/TEGDMA dental composite incorporated with ZnO/CS and Si/PMMA core–shell nanostructures

Izel Ok[1] · **Ahmet Aykac**[1,2]

Received: 27 April 2023 / Accepted: 15 July 2023 / Published online: 26 July 2023

Abstract
In this study, Si/PMMA and ZnO/CS core–shell structures were synthesized as inorganic fillers and added to a bisphenol A diglycidyl dimethacrylate (Bis-GMA)/triethylene glycol dimethacrylate (TEGDMA) (50%/50%) commercial dental composite at a weight percentage (wt%) of 0.1–1.0% to simultaneously improve the mechanical and antibacterial properties of the composite. The prepared composites were characterized using dynamic light scattering (DLS), zeta potential (ζ-potential), Fourier transform infrared spectroscopy (FTIR), scanning electron microscope (SEM), ultraviolet–visible spectrophotometer (UV–Vis), thermogravimetric analysis (TGA), X-ray photoelectron spectroscopy (XPS), and X-ray powder diffraction (XRD). The mechanical properties, including flexural strength and flexural modulus, of the composite were investigated by three-point bending tests. Additionally, the antibacterial activity against the *Staphylococcus aureus (S. aureus)* bacteria strain was evaluated using the colony-forming unit method to assess the antibacterial effect of the novel composite. As a result, the Bis-GMA/TEGDMA-Si/PMMA/ZnO/CS dental composite, reinforced with 0.1 wt% Si/PMMA and 0.5 wt% ZnO/CS, exhibited a 46% improvement in flexural strength and a 56% improvement in flexural modulus compared to pristine Bis-GMA/TEGDMA. Moreover, the novel Bis-GMA/TEGDMA-Si/PMMA/ZnO/CS dental composite showed a 95% reduction in bacterial growth against the *S. aureus* bacteria strain.

Extended author information available on the last page of the article

Graphical Abstract

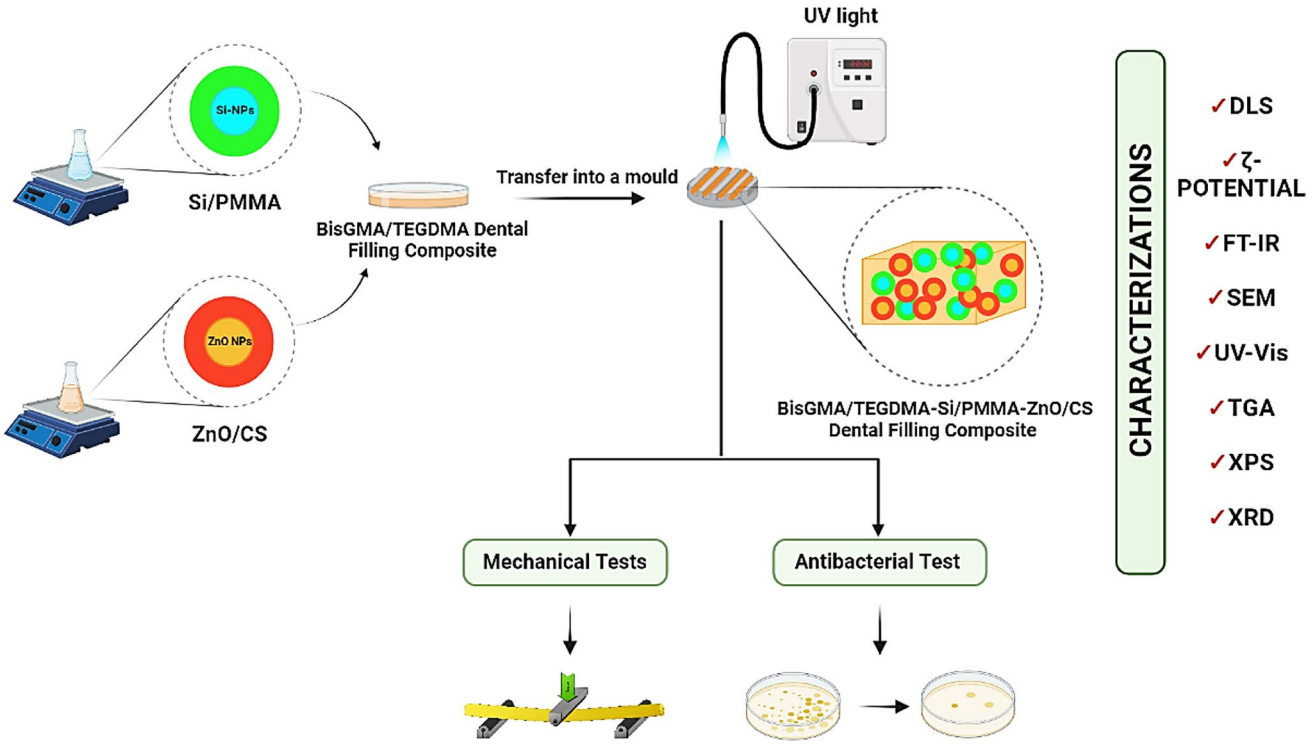

Keywords Bis-GMA/TEGDMA · Dental filling composite · Si/PMMA · ZnO/CS · Core–shell · Mechanical strength · Antibacterial properties

Introduction

Over the past century, the dental field has witnessed significant advancements through the adoption of resin-based composite technology in dentistry. Dental composite resins have gained popularity as materials for tooth restorations due to their aesthetic appeal, superior wear resistance, and ease of application, especially when compared to dental amalgams (Alzraikat et al. 2018). However, it is important to note that these composites deteriorate over time, leading to the emergence of cracks and fractures. This deterioration primarily stems from their inherent characteristics of low strength, high brittleness, and polymerization shrinkage, as highlighted in studies conducted by researchers (Chen et al. 2012; Cetin et al. 2013; Kundie et al. 2018). Nanoparticles (NPs) with sizes ranging from 1 to 100 nm and their large surface areas have been utilized in dental composites to mitigate polymerization shrinkage and enhance mechanical properties such as tensile strength and pressure, thereby improving durability and fracture resistance (Karabela and Sideridou 2011). Dental composites used in restorations typically consist of three main components: (1) various types, shapes, and sizes of inorganic filler materials, (2) an organic matrix that supports the inorganic filler, and (3) a silane coupling agent that binds the organic and inorganic components together. The most used organic matrix material is bisphenol A diglycidyl dimethacrylate (Bis-GMA), which has a highly viscous structure due to the presence of hydroxyl groups and the π–π interactions provided by aromatic rings. Bis-GMA is often combined with low-viscosity monomers like triethylene glycol dimethacrylate (TEGDMA) to reduce viscosity and improve processing properties (Gajewski et al. 2012). The interphase, which is composed of silane-derived coupling agents, strengthens the adhesion between the different phases of organic matrix and inorganic fillers, affects the aggregation degree of filler particles, and facilitates stress transfer between the stronger filler phase and the weaker matrix phase (Wilson and Antonucci 2006). Studies have shown that the particle morphology (shape), size range, and volume content of dental composites have a significant impact on their mechanical properties and aesthetic appearance (Canché-Escamilla et al. 2014; Alzraikat

et al. 2018). The characteristic properties of dental composites are greatly influenced by the distribution of nano-sized filling particles. However, controlling the dispersion of these NPs in the polymeric matrix is challenging as they tend to agglomerate due to their high surface area and the surface charge of the inorganic NPs. In order to control the dispersion of these NPs and enhance the interfacial adhesion between the particles and the polymer, core–shell nanostructures, where the inorganic particles are surrounded by a polymer shell, have been synthesized. One of these nanostructures is the Si/PMMA core–shell nanostructure, composed of silica NPs (Si-NPs) and polymethylmethacrylate (PMMA).

Silica is widely used as an inorganic filler in the preparation of dental composites due to its favourable physical and chemical properties, including good mechanical strength and non-toxicity (Canché-Escamilla et al. 2014). PMMA is another commonly used materials in dental applications due to its biocompatibility, and low cost (Elizalde-Peña et al. 2007; Zaharia et al. 2016). Silane coupling agents play a crucial role in facilitating the covalent bonding between PMMA and silica nodes (Harb et al. 2016). Kim et al. produced the silica/PMMA core–shell nanostructure using ɣ-methacryloxy propyl trimethoxy silane (ɣ-MPS) as the silane coupling agent (Kim et al. 2013), while Canché-Escamilla et al. (2014) reinforced the Bis-GMA/TEGDMA dental composite by incorporating Si/PMMA core–shell nanostructures. Chitosan (CS) is a modified natural carbohydrate polymer and linear cationic polysaccharide obtained through alkaline deacetylation of chitin (Haldorai and Shim 2013; Zhao et al. 2018; Javed et al. 2020). Due to its general instability, studies have explored composites of CS with metal oxides such as zinc oxide (ZnO) NPs. Researches on ZnO/CS composites have demonstrated significant enhancement of the antibacterial and antibiofilm properties of ZnO NPs through a synergistic effect with CS (Salehi et al. 2010; Haldorai and Shim 2013; Buşilă et al. 2015). For instance, Javed et al. reported that encapsulating ZnO NPs with CS increased their antibacterial properties (Javed et al. 2020).

The oral cavity harbours various microorganisms, including bacteria and fungi, which can lead to plaque biofilm, dental caries, periodontitis, and other dental infections. In recent years, nanomaterials have been extensively utilized to enhance the antibacterial properties of dental composites (Song and Ge 2019). Studies in the literature have explored the use of nanomaterials such as imidazole and benzimidazole NPs (Kaptan Usul et al. 2022), chlorhexidine/amorphous calcium phosphate (CHX/ACP) NPs (Yang et al. 2021), silver NPs derived from Mangifera indica leaves (Sundeep et al. 2017), and bismuth subsalicylate (BSS) NPs (Vega-Jiménez et al. 2017) to improve the antibacterial characteristics of dental composites. Among the pathogens associated with dental infections, *Staphylococcus aureus (S. aureus)*, a Gram-positive bacterium known for its antibiotic resistance and involvement in dental infections, is commonly encountered (Wang and Ren 2017) and several studies conducted in dental clinics have focused on *S. aureus*. One notable study conducted by Al-Shamahy and Al-labani involved a year-long clinical investigation with 296 participants of varying ages and genders. Their findings concluded that *S. aureus* is one of the predominant antibiotic-resistant bacterial strains responsible for dental infections (Al-Shamahy and Al-labani 2020). Similarly, McCormack et al. conducted a study utilizing 10 years of oral and perioral clinical laboratory data on *S. aureus*, highlighting its prevalence as an oral and perioral isolate associated with distinct oral infections and exhibiting antibiotic resistance (McCormack et al. 2015).

To address the mechanical and antibacterial challenges associated with dental filler composites (DFC), we developed a novel dental composite by incorporating the Si/PMMA core–shell nanostructure (0.1–0.5 wt%) and ZnO/CS core–shell nanostructure (0.1–1.0 wt%) into the commonly used Bis-GMA/TEGDMA (50%/50% wt%) dental organic matrix. The mechanical properties of the composite, specifically flexural strength and flexural modulus were evaluated through a three-point bending test. Additionally, the antibacterial activity of the composite was assessed against the *S. aureus* bacteria strain. To the best of our knowledge, this study represents the first investigation in which Si/PMMA and ZnO/CS components were synthesized, characterized, and incorporated into the structure of a dental composite as inorganic fillers. The incorporation of these core–shell nanostructures resulted in improved mechanical properties and enhanced antibacterial activity. Consequently, the developed dental composite has the potential to hinder the formation of new caries while exhibiting increased strength and resistance to biting and chewing pressures.

Materials and methods

Materials

Tetraethyl orthosilicate (TEOS), ammonium hydroxide solution (NH_4OH), absolute ethanol ($C_2H_5OH, > 99.7\%$), 3-(Trimethoxysilyl)propyl methacrylate (MPTS), methyl methacrylate (MMA), hexadecyltrimethylammonium bromide (CTAB), potassium persulfate ($K_2S_2O_8$, 99 + %), calcium chloride ($CaCl_2$), zinc acetate dihydrate ($Zn(CH_3COO)_2{\cdot}2H_2O$), sodium hydroxide (NaOH), low molecular weight chitosan (CS, low MW), acetic acid (CH_3COOH), bisphenol A glycerolate dimethacrylate (Bis-GMA), triethylene glycol dimethacrylate (TEGDMA), ethyl

4-dimethylaminobenzoate (4EDMAB, 99%), and camphorquinone (CQ, 97%) were obtained from Sigma Aldrich. Distilled water (DI water) was used throughout the study. All chemicals utilized were of analytical grade and used as received without any additional purification.

Synthesis and surface modification of non-porous silica nanoparticles and preparation of Si/PMMA core–shell nanostructure

Non-porous silicon nanoparticles (Si-NPs) were synthesized using a modified version of the Stöber method, which is a widely recognized technique for Si-NP production (Şen Karaman et al. 2014). In this procedure, 8.6 mL of TEOS was added to 200 mL of C_2H_5OH, and then, 12 mL of NH_4OH was added dropwise to mixture. The resulting solution was stirred at room temperature for 12 h. Afterwards, the solution was washed with C_2H_5OH at 7500 rpm for 3 cycles of 30 min each. For the surface modification (silanization) of Si-NPs, 100 mg of the synthesized Si-NPs was dispersed into the 3.3 mL of C_2H_5OH for 45 min using an ultrasonic bath. Then, 83 mg of MTPS as a silane coupling agent were added to the solution and the dispersion was maintained in the ultrasonic bath for 2.5 h. The collected particles were subsequently washed with C_2H_5OH at 7500 rpm for 3 cycles of 30 min each (Zhang et al. 2012). The chemical reaction steps are depicted in Fig. 1a.

The synthesis of the Si/PMMA core–shell (50/50) nanostructure was performed through emulsion polymerization of MMA on the silanized Si-NPs. In this process, 220 mg of CTAB as a surfactant and a certain amount of silanized Si-NPs were mixed in 8 mL of DI water in a reaction vessel under vigorous stirring at 50 °C for 2 h. Subsequently, 120 mg of KPS and certain amount of MMA monomer were added to the solution and the stirring was continued at 80 ± 0.5 °C for 1 h. After completion, the solution was allowed to cool to room temperature. The resulting white solution was then precipitated using a 0.1 M $CaCl_2$ aqueous solution and the particles were washed with DI water at 7500 rpm for 3 cycles of 30 min each. Finally, the particles were dried at 60 °C overnight. The chemical reaction steps are illustrated in Fig. 1b (Yang and Dan 2003).

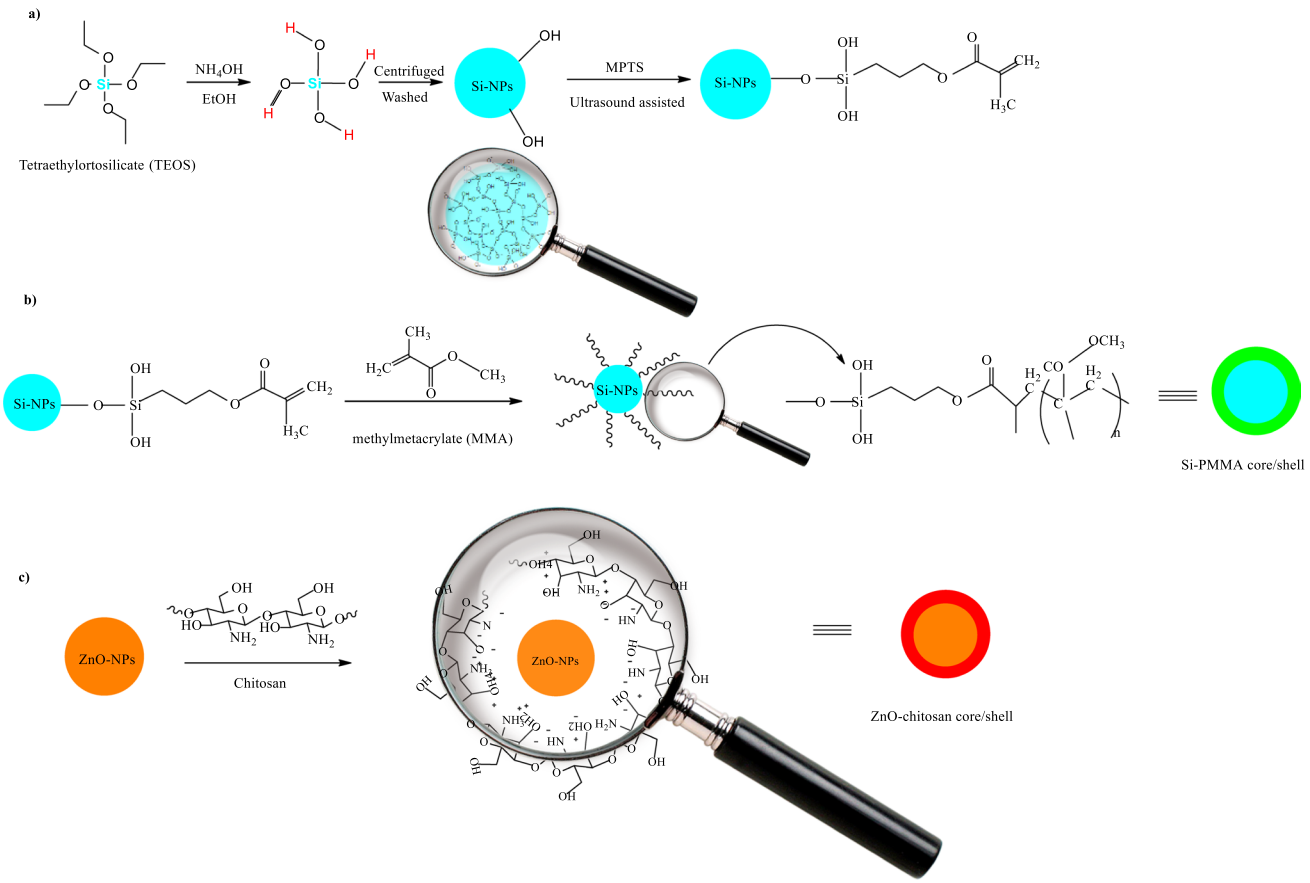

Fig. 1 Schematic illustration of **a** Si@MPTS-NPs, **b** Si/PMMA core–shell nanostructure, and **c** ZnO/CS core–shell nanostructure

Synthesis of zinc oxide nanoparticles and ZnO/CS core–shell nanostructure

The synthesis of ZnO NPs was performed using the precipitation method. This method involves the precipitation of Zn ions in a suitable solvent or solution under controlled conditions. By introducing a precipitating agent or changing the pH of the solution, Zn ions undergo a chemical reaction leading to the formation of ZnO NPs (Gnanasangeetha and Saralathambavani 2013). To carry out the synthesis, 876 mg of $Zn(CH_3COO)_2{\cdot}2H_2O$ was dissolved in 200 mL of DI water at room temperature. Next, a 2 M NaOH solution was added dropwise to the solution until the pH reached 11. The reaction mixture was stirred at room temperature for 2 h. After the reaction, the ZnO NPs were washed with DI water through centrifugation at 7500 rpm for 3 cycles of 30 min each. Subsequently, the washed NPs were dried at 60 °C overnight to obtain the final product of ZnO NPs.

The ZnO NPs were coated with CS through electrostatic interaction, following the method (Javed et al. 2020). In this process, 100 mg synthesized of ZnO NPs were dissolved in 10 mL of 1% (v/v) CH_3COOH solution. Then, 100 mg of CS (low MW) was added to the solution, and the reaction mixture was placed in an ultrasonic bath at 40 °C for 20 min. Next, a 1 M NaOH solution was added dropwise to the mixture until the pH reached 11, and the reaction was stirred at 65 °C for 3 h. After the completion of the reaction, the particles were washed with DI water at 7500 rpm for 3 cycles of 30 min each and then dried at 60 °C overnight to obtain ZnO/CS core–shell nanostructures (Fig. 1c) (Dananjaya et al. 2018).

Preparation of Si/PMMA and ZnO/CS modified Bis-GMA/TEGDMA dental filling composites

In order to evaluate the effect of Bis-GMA/TEGDMA ratios on the mechanical properties of the composite, different formulations of Bis-GMA/TEGDMA DFC were prepared without Si-based and ZnO-based additives. The ratios of Bis-GMA to TEGDMA used were 30%/70%, 40%/60%, and 50%/50% (wt%). The preparation of the DFC involved the following steps:

(a) Heating of high viscosity Bis-GMA: the high viscosity Bis-GMA component was heated in an ultrasonic bath for 45 min. This step helps to reduce the viscosity of the Bis-GMA resin, making it easier to handle and mix with other components.
(b) Addition of TEGDMA and photoinitiators: TEGDMA monomer and the photoinitiators, CQ (0.2 wt%) and 4EDMAB (0.8 wt%), were weighed in the dark. They were then added to the Bis-GMA resin matrix and were mixed in the ultrasonic bath for 3 h at 40 °C in the dark. This mixing ensures uniform distribution of the monomers and initiators within the resin matrix.
(c) Pouring into a mould and curing: the resulting mixture was poured into a Teflon mould with dimensions of 2 mm × 2 mm × 25 mm, following the ISO 4049-2000 "dentistry-polymer-based restorative materials" standard. The mould provides the desired shape and dimensions for the test specimens. The filled mould was cured for 2 min under a 365 nm UV light source with a density of 7 mW/cm^2 (Karabela and Sideridou 2011; Canché-Escamilla et al. 2014). The UV light activates the photoinitiators, initiating the polymerization process and curing the resin.

The same preparation method was followed for the DFC that included Si@MPTS-NPs, Si/PMMA core–shell, and Si/PMMA/ZnO/CS core–shell nanostructures. The nanostructures were incorporated into the resin matrix along with the Bis-GMA and TEGDMA components before mixing and curing.

Instruments and characterization

The synthesized Si-NPs, Si@MPTS-NPs, Si/PMMA core–shell, ZnO NPs, and ZnO/CS core–shell nanostructures were subjected to various characterizations. The hydrodynamic particle sizes and surface charges of the NPs were determined using dynamic light scattering (DLS) and zeta potential (ζ-potential) *(Anton Paar Litesizer 500, Particle Analyzer)* measurements. Fourier transform infrared spectroscopy (FTIR) *(Thermo scientific nicolet is50 FTIR)* was employed to confirm the qualitative structural characteristics of the synthesized NPs in the range of 400–4500 cm^{-1}. The morphology and size of the NPs were observed using scanning electron microscope (SEM) *(Carl Zeiss 300VP)*. The absorbance properties of the NPs were measured using ultraviolet–visible spectrophotometer (UV–Vis) *(Thermo Scientific Evolution 201 UV–Visible Spectrophotometer)* in the wavelength range of 280–600 nm. The thermal stability of the NPs was assessed by thermogravimetric analysis (TGA) *(TA TGA-SDT Q600)* conducted under a nitrogen atmosphere with a heating rate of 10 °C/min in the temperature range of 30–800 °C. X-ray photoelectron spectroscopy (XPS) *(Thermo Scientific K-Alpha)* analysis was performed to determine the elemental composition and structure of the NPs. X-ray diffraction (XRD) (*Thermo Scientific ARL X'TRA)* analysis using Cu (Kα) radiation ($\lambda = 0.15418$ nm) was carried out for the characterization of ZnO and ZnO/CS NPs, with a 2°/min scanning speed in the range of $3 \leq 2\theta \leq 90°$. These characterization techniques provided valuable information regarding the particle size, surface charge, morphology, absorbance, qualitative nanostructures, thermal

stability, elemental composition, and crystal structure of the synthesized NPs.

Mechanical tests

To assess the mechanical properties of the DFC, flexural strength and flexural modulus tests were conducted. The samples were prepared in accordance with the ISO 4049-2000 standard titled 'Dentistry-Polymer-based restorative materials.' Composite material was poured into Teflon moulds with dimensions of 2 mm × 2 mm × 25 mm and cured under UV light. Prior to the tests, the samples were stored overnight in DI water in the dark. Mechanical tests were performed on at least three samples for each dental composite material using a universal tester (SHIMADZU AG-IC) at a cross-head speed of 1 mm/min. The three-point bending test configuration is shown in Fig. S1a, b depicts the composite parts obtained after the three-point bending test. The mechanical strength of Si/PMMA and ZnO/CS modified DFC was evaluated by conducting experiments with different ratios of the components in two steps, as illustrated in Fig. 2. The best results obtained in each row are represented by the green boxes, and for each subsequent row, the green box from the previous row was selected for the next step.

In vitro antibacterial activity assays

In vitro antibacterial activity assays were conducted using *S. aureus* bacteria strain. The bacterial suspensions were obtained from stock culture stored at − 80 °C. The strains were cultivated in tryptic soy agar (TSA) medium and incubated at 37 °C overnight (16–18 h). After the incubation, a single colony was isolated, seeded in tryptic soy broth (TSB), followed by overnight incubation at 37 °C. The bacteria were then centrifuged, and the resulting pellet was suspended in phosphate buffer saline (PBS) to achieve a concentration of approximately 10^6 CFU/mL (600 nm: 0.6–0.8 optical density). Each application was prepared by diluting the bacterial suspension to 10^5 CFU/mL. The DFC were added to the *S. aureus* bacterial solution and incubated overnight at 37 °C. Subsequently, the colony counting method was employed for all groups (Taslı et al. 2018). In this method, 100 µL of the incubated solution was taken, diluted using a serial dilution technique, and spread onto TSA medium. The plates were then incubated at 37 °C overnight (16–18 h). The resulting colonies on the agar were counted and the ratio of colonies to the total solution volume was calculated. Each experimental group was compared with its corresponding control group.

Result and discussion

Characterizations

Figure 3a, b depicts the results of DLS and ζ-potential analyses for Si-NPs, Si@MPTS-NPs, and Si/PMMA core–shell nanostructures. The hydrodynamic diameter of non-porous Si-NPs and Si@MPTS-NPs was found to be approximately 98 nm and 110 nm, respectively (Şen Karaman et al. 2014). The ζ-potential values of these NPs were negative (−) and the surface charges of the Si-NPs approached neutrality after silanization at pH 7. Although the particle size did not show a significant change after silanization, the alteration in ζ-potential values indicated the successful synthesis of the reaction and the presence of an interaction between Si-NPs and MPTS silane agents. The thickness of the silane layer has a significant effect on the efficiency of the silanization process, and the layers become more irregular as the silane thickness increases. Therefore, the negligible increase in particle size after silanization was interpreted as a positive outcome in terms of particle quality (El-Banna et al. 2019). The Si/PMMA core–shell nanostructure exhibited NPs size of approximately 250 nm. The surface charges of

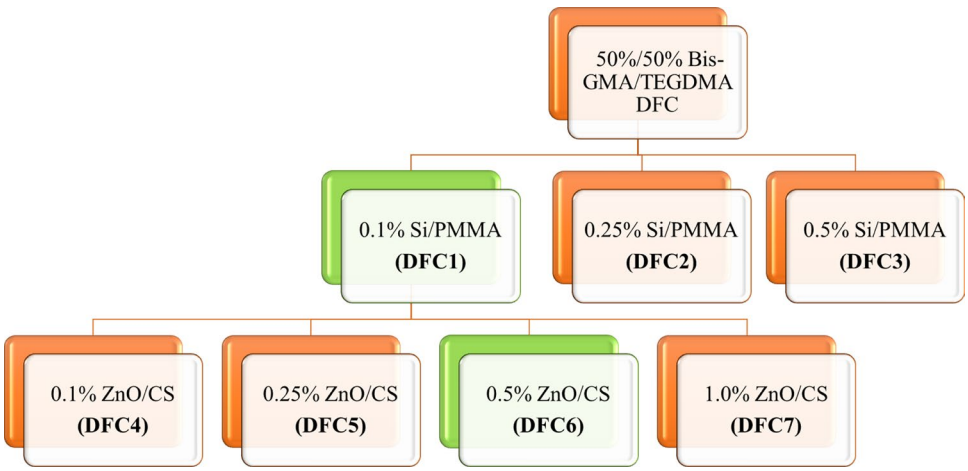

Fig. 2 The composition of Bis-GMA/TEGDMA DFC with Si/PMMA and ZnO/CS core–shell nanostructures

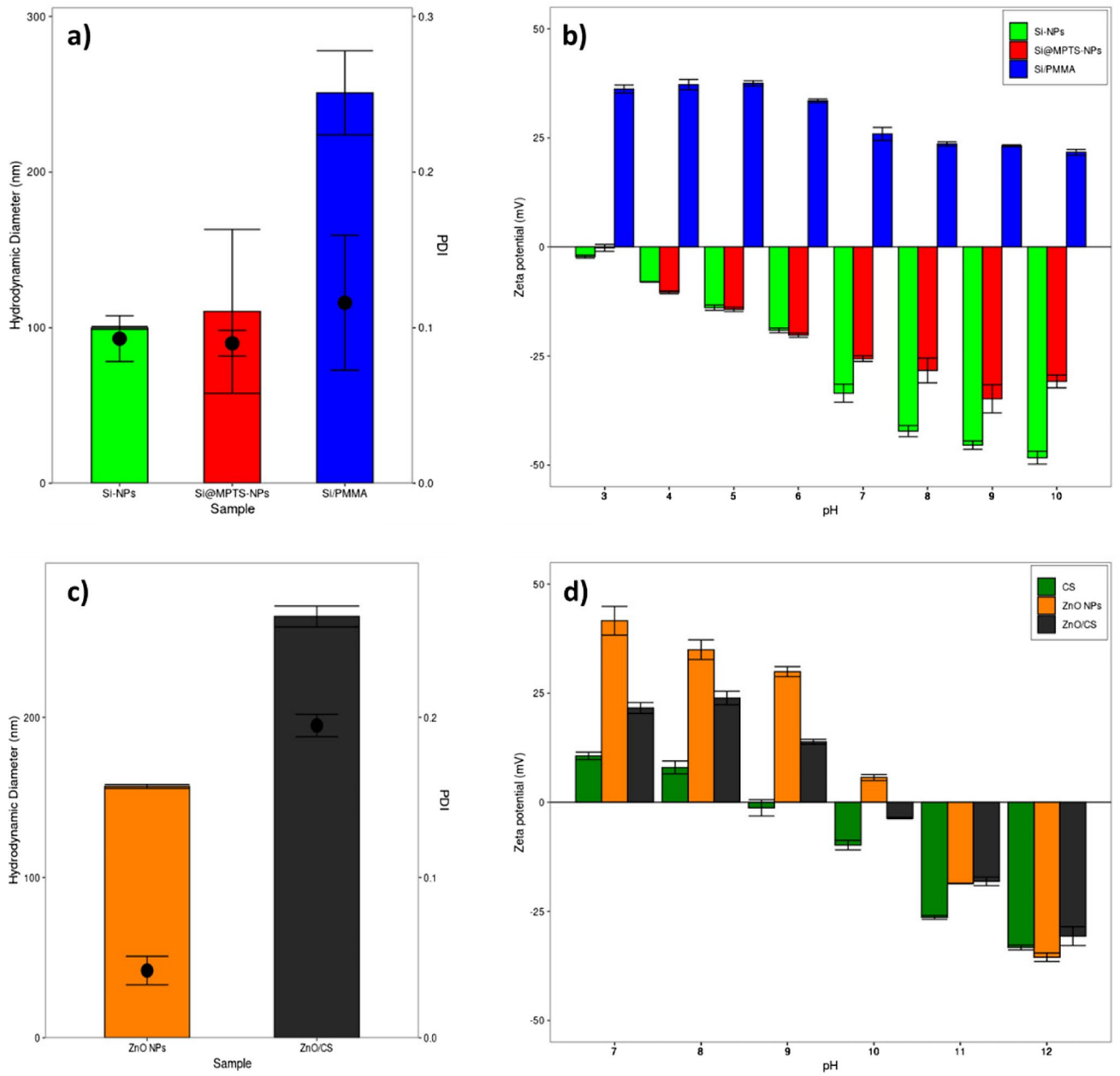

Fig. 3 **a** The hydrodynamic size and PDI of Si-NPs, Si@MPTS-NPs, **b** ζ-potential of and Si/PMMA core–shell nanostructure, **c** the hydrodynamic size and PDI of ZnO NPs and ZnO/CS core–shell nanostructure, and **d** ζ-potential of ZnO NPs and ZnO/CS core–shell nanostructure

Si-NPs and Si@MPTS-NPs were negative (−), while the Si/PMMA core–shell nanostructure showed positive (+) surface charges. This positive charge can be attributed to the use of cationic CTAB surfactant during the polymerization reaction (Khademi et al. 2017). These NPs exhibited low polydispersity index (PDI), typically less than 0.1. This low PDI value further confirmed the monodisperse distribution of the NPs. A low PDI indicates a narrow size distribution, with minimal variation in particle sizes, supporting the observation of monodispersity in the NPs (Petrizza et al. 2016). Regarding the DLS and ζ-potential analyses of ZnO NPs (Fig. 3c) and ZnO/CS core–shell nanostructure (Fig. 3d), the hydrodynamic diameter of ZnO NPs was around 160 nm and PDI was 0.04, while the hydrodynamic diameter of the ZnO/CS core–shell nanostructure was approximately 270 nm and PDI was 0.19 (Dananjaya et al. 2018). The ζ-potential of ZnO NPs was found to be positive (+) between pH 7 and pH 10, which corresponds to the isoelectric point of ZnO NPs. At pH 11 and pH 12, the ζ-potential of ZnO turned negative (Zhang et al. 2013). After the formation of the core–shell structure, the ζ-potential of ZnO/CS decreased, which indicates a change in the surface charge characteristics, which

Table 1 The hydrodynamic diameter (nm), polydispersity index (PDI), and ζ-potential (mV) pH:7 results of the synthesized NPs

Sample	Hydrodynamic Diameter (nm)	Polydispersity index (PDI)	ζ-potential (mV) pH:7
Si-NPs	98 nm	0.09	−33.5
Si@MPTS-NPs	110 nm	0.08	−25.6
Si/PMMA	250 nm	0.12	25.9
ZnO NPs	160 nm	0.04	41
ZnO/CS	270 nm	0.19	21

can be attributed to the presence of the CS shell encapsulating the ZnO NPs. This change in surface charge provided additional confirmation of the formation of the core–shell structure (Swain et al. 2009). The average results of the DLS, PDI, and ζ-potential measurements are given in Table 1.

The FTIR spectra of Si-NPs, Si@MPTS-NPs, Si/PMMA core–shell nanostructures, ZnO NPs, and ZnO/CS nanostructures are shown in Fig. S2a to confirm the qualitative structural confirmation of the synthesized NPs. Additionally, Fig. S2b specifically displays the FTIR spectra of ZnO NPs, and ZnO/CS nanostructures.

The SEM images presented in Fig. 4a–c depict the Si-NPs, Si/PMMA core–shell nanostructure, and ZnO/CS core–shell nanostructures, respectively. These SEM images clearly show that the NPs are predominantly monodisperse, exhibiting uniform sizes and well-defined spherical shapes. These visual observations strongly support the results obtained from the DLS analysis regarding the monodispersity of the particles (Şen Karaman et al. 2014; Canché-Escamilla et al. 2014; Nguyen et al. 2020).

The UV–Vis spectra of pristine Si-NPs, Si@MPTS-NPs, Si/PMMA core–shell nanostructures are depicted in Fig. S3a, while the UV–Vis spectra of ZnO NPs and ZnO/CS core–shell nanostructures are presented in Fig. S3b.

According to TGA analyses, Si-NPs and Si@MPTS-NPs showed decomposition of approximately 5–10% at 122 °C, whereas the Si/PMMA core–shell nanostructure exhibited decomposition at 156 °C and 186 °C as shown

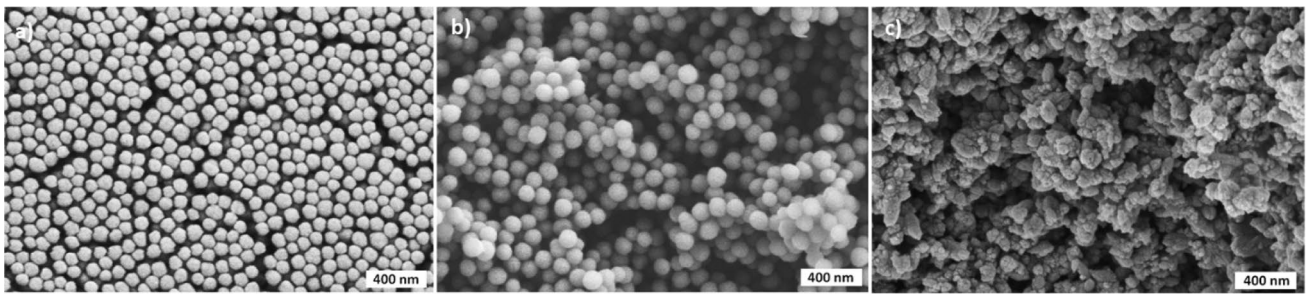

Fig. 4 SEM images of **a** Si-NPs, **b** Si/PMMA core–shell nanostructure, and **c** ZnO/CS core–shell nanostructures

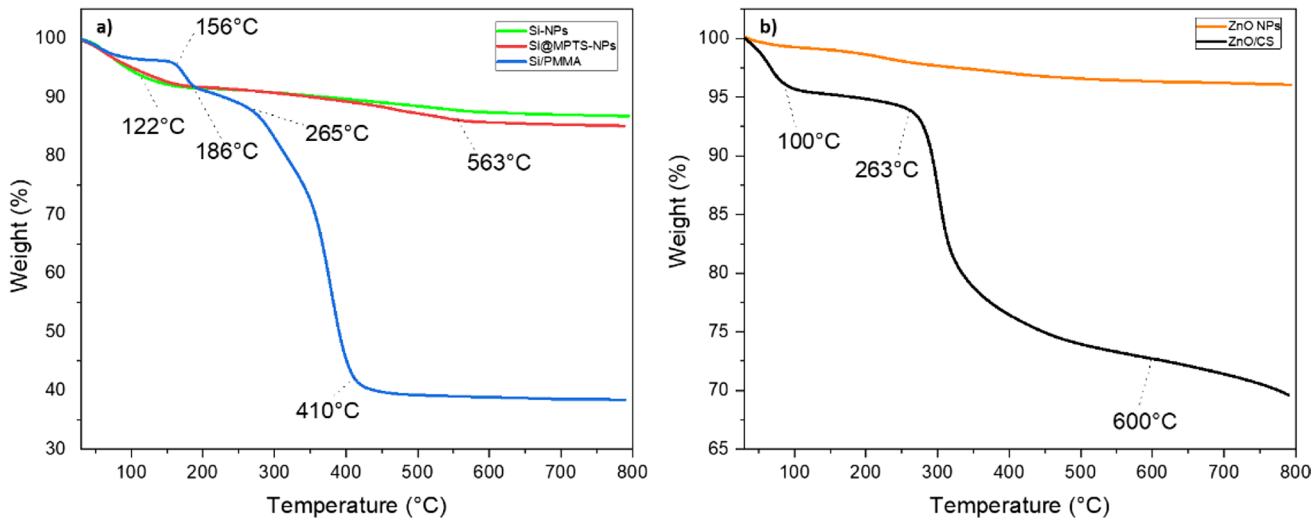

Fig. 5 **a** TGA analysis of Si-NPs, Si@MPTS-NPs, Si/PMMA core–shell nanostructure, **b** TGA analysis of ZnO NPs, and ZnO/CS core–shell nanostructures

in Fig. 5a. This was possibly due to moisture content in the materials. Since Si-NPs and Si@MPTS-NPs were homogeneous, no major decomposition was observed with increasing temperature. Approximately 5% of the weight of Si@MPTS-NPs was lost at 563 °C. High temperature was required to decompose and evaporate the organic content of Si@MPTS-NPs. This indicated the presence of a strong covalent bond between the silane coupling agent and the surface of Si-NPs (Zhang et al. 2012). The decomposition of the Si/PMMA core–shell nanostructure was more significant, with about 35% weight loss occurring between 265 and 410 °C, attributed to the decomposition of PMMA. However, the presence of silica in the nanostructure prevented complete degradation (Yang and Dan 2003; Zhang et al. 2012). In the case of ZnO NPs, TGA analysis showed minimal weight loss, less than 5%, and a stable weight up to 800 °C, indicating their high thermal stability as depicted in Fig. 5b. The slight weight loss observed was attributed to the removal of surface moisture. Due to the homogeneous nanostructure of ZnO NPs, a significantly higher temperature was required for their complete dissociation. On the other hand, the ZnO/CS core–shell nanostructure exhibited around 5% decomposition at 100 °C, related to the removal of surface moisture. The main degradation of the ZnO/CS nanostructure occurred between 263 and 600 °C, resulting in a total weight loss of approximately 20% in this temperature range. Beyond 600 °C, the weight loss continued at a slower rate, with an additional 5% reported (Masud et al. 2020; Nguyen et al. 2020).

Figure 6 presents the wide scan XPS spectra of Si-based NPs and ZnO-based NPs. In the C1s spectrum, four components were identified, representing C–H, C–C–O, C–O, and O–C=O bonds present in the PMMA and MPTS molecules (Harb et al. 2016). The wide scan XPS spectra of Si/PMMA core–shell nanostructure exhibited a strong signal corresponding to the C–C/C–H aliphatic hydrocarbon at a binding energy of 285 eV. This peak exhibited higher intensity compared to the C1*s* signal of Si-NPs and Si@MPTS-NPs, indicating the presence of PMMA on the surface of silica. Regarding the O1*s* signal at a binding energy of 533 eV, the O1s signals of Si-NPs and Si@MPTS-NPs were attributed to the Si–O bond. However, the O1*s* signal of the Si/PMMA core–shell nanostructure was weaker and corresponded to the carbonyl oxygen (O=C) of MMA. The Si2*p* signal, with a well-known binding energy of approximately 103.5 eV, exhibited a shift in Si@MPTS and Si/PMMA, likely due to the presence of Si–OH groups remaining from TEOS and MPTS hydrolysis. On the other hand, the Si2*p* signal of Si-NPs and Si@MPTS-NPs was significantly stronger than Si/PMMA core–shell nanostructure, as the Si-NPs served as the core encapsulated by the PMMA shell (Zhang et al. 2012; Harb et al. 2016). Moving to the XPS spectra of ZnO-based NPs, two peaks were observed at 1022 eV and 1045 eV, corresponding to the binding energies of Zn2*p*3/2 and Zn2*p*1/2 lines, respectively. The O1*s* spectrum exhibited a single peak at 532 eV, which can be attributed to O^{+2} ions in ZnO NPs. The C1*s* spectrum appeared at 285 eV and 286 eV (Chang et al. 2019). These XPS spectra provide valuable information about the chemical composition and bonding states of the NPs, shedding light on their surface properties and potential applications.

The XRD results of ZnO NPs and ZnO/CS core–shell are presented in Fig. 7. The XRD pattern of ZnO NPs exhibited prominent diffraction peaks at specific angles, including 31.92° (1 0 0), 34.52° (0 0 2), 36.42° (1 0 1), 47.56° (1 0 2), 56.52° (1 1 0), 62.88° (1 0 3) and 67.98° (1 1 2). These peaks corresponded to the characteristic hexagonal wurtzite crystal structure of ZnO NPs. On the other hand, the XRD pattern of the ZnO/CS core–shell nanostructure exhibited similar peaks to that of ZnO NPs, indicating the presence of ZnO as the main component. However, the intensity of the peaks in the ZnO/CS core–shell nanostructure was relatively lower compared to the pure ZnO NPs. This decrease in intensity was attributed to the interactions between ZnO and CS. Despite these interactions, the crystal structure of ZnO remained intact, and the appearance of two sets of diffraction peaks corresponding to ZnO and CS confirmed the successful formation of the ZnO/CS core–shell nanostructure. Furthermore, the absence of zinc (Zn) peaks in the medium indicated the high purity of the synthesized ZnO NPs and ZnO/CS core–shell nanostructures (Ahmed et al. 2018; Dananjaya et al. 2018). In Fig. 7, the peaks indicated by (a) represent the characteristic peaks of CS, while the peaks indicated by (b) correspond to the peaks of the ZnO nanostructure (Kumar and Koh 2012).

Mechanical tests

In this study, the mechanical tests were conducted to evaluate the performance of different compositions of Bis-GMA/TEGDMA DFC. Based on the characterization results, the 50%/50% Bis-GMA/TEGDMA composition was chosen for further investigation. The flexural strength and flexural modulus of the pristine Bis-GMA/TEGDMA DFC were found to be 39.80 MPa and 692.07 MPa, respectively, as determined by the three-point bending test. To improve the mechanical properties of the DFC, different wt% of Si/PMMA nanostructure were incorporated. The best results were obtained with 0.1% Si/PMMA additive (DFC1), as shown in Fig. 8a, b. The flexural strength of DFC1 increased to 66.73 MPa, a 68% improvement compared to the pristine DFC. Similarly, the flexural modulus increased to 1091.82 MPa, a 58% improvement. Furthermore, different wt% ratios of ZnO/CS core–shell nanostructures were added to DFC1, resulting in DFC4, DFC5, DFC6, and DFC7 samples. The best

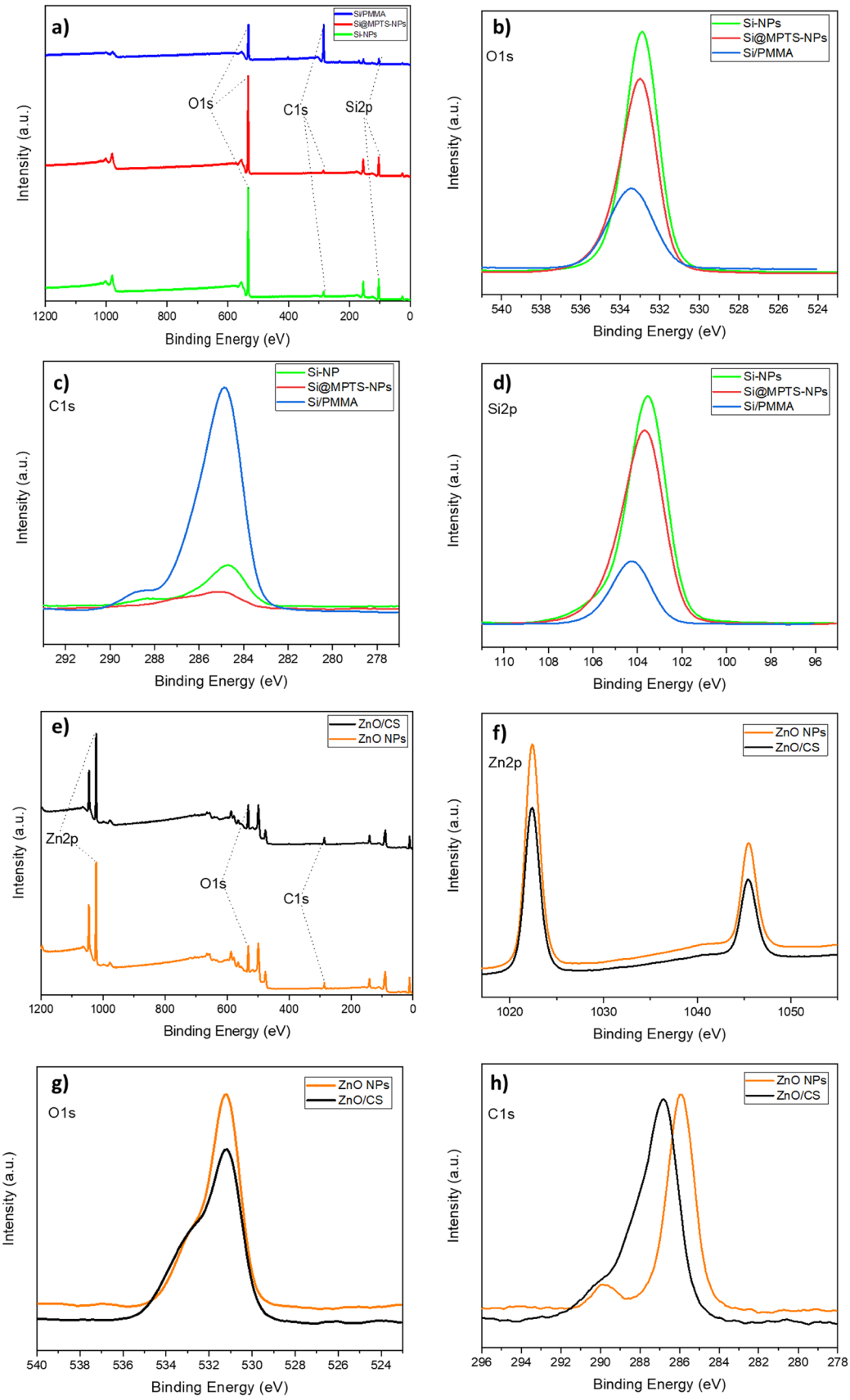
a)
Si/PMMA
Si@MPTS-NPs
Si-NPs
O1s
C1s
Si2p
Intensity (a.u.)
Binding Energy (eV)
b)
O1s
Si-NPs
Si@MPTS-NPs
Si/PMMA
Intensity (a.u.)
Binding Energy (eV)
c)
C1s
Si-NP
Si@MPTS-NPs
Si/PMMA
Intensity (a.u.)
Binding Energy (eV)
d)
Si2p
Si-NPs
Si@MPTS-NPs
Si/PMMA
Intensity (a.u.)
Binding Energy (eV)
e)
ZnO/CS
ZnO NPs
Zn2p
O1s
C1s
Intensity (a.u.)
Binding Energy (eV)
f)
Zn2p
ZnO NPs
ZnO/CS
Intensity (a.u.)
Binding Energy (eV)
g)
O1s
ZnO NPs
ZnO/CS
Intensity (a.u.)
Binding Energy (eV)
h)
C1s
ZnO NPs
ZnO/CS
Intensity (a.u.)
Binding Energy (eV)

◂**Fig. 6** XPS spectra of **a** Si-based NPs survey, **b** O1*s* spectra of Si-based NPs, **c** C1*s* spectra of Si-based NPs, **d** Si2*p* spectra of Si-based NPs, **e** ZnO-based NPs survey, **f** Zn2*p* spectra of ZnO-based NPs, **g** O1*s* spectra of ZnO-based NPs, and **h** C1*s* spectra of ZnO-based NPs

results were obtained with DFC6, which contained 0.1% Si/PMMA and 0.5% ZnO/CS core–shell nanostructures, as shown in Fig. 8c, d. DFC6 exhibited a flexural strength of 58.05 MPa, a 46% improvement, and a flexural modulus of 1077.75 MPa, a 56% improvement compared to the pristine Bis-GMA/TEGDMA. It was observed that both the flexural strength and flexural modulus increased with the addition of ZnO/CS core–shell additives up to 0.5 wt%. However, the mechanical properties started to decrease when the additive content exceeded 0.5 wt%. These findings demonstrate that the incorporation of Si/PMMA and ZnO/CS core–shell nanostructures can significantly enhance the mechanical properties of the Bis-GMA/TEGDMA DFC composition.

In vitro antibacterial activity assays

The in vitro antibacterial activity assays were conducted to evaluate the antibacterial properties of Si-NPs, Si/PMMA core–shell nanostructure, ZnO NPs, ZnO/CS core–shell nanostructure, and Bis-GMA/TEGDMA dental composites with different additives against *S. aureus* strain. The results are presented in Fig. 9a–c. Si-NPs exhibited a 67% antibacterial activity against the *S. aureus* strain, while the Si/PMMA core–shell nanostructure showed an 84% antibacterial activity. Although the antibacterial activities of Si-NPs are not commonly reported in the scientific literature, Agnihotri et al. (2015) mentioned minor antibacterial activity of Si-NPs against *S. aureus* bacteria. Similarly, Sodagar et al. evaluated the antibacterial effect of PMMA with SiO_2 NPs and TiO_2 NPs and reported a 51% antibacterial activity of Si/PMMA nanostructure against *Streptococcus mutans* and a 67% antibacterial activity against *Lactobacillus acidophilus* (Sodagar et al. 2016). ZnO NPs and ZnO/CS core–shell nanostructures exhibited significant antibacterial activity against *S. aureus* at 98% and 92%, respectively (Fig. 9b). Several studies in the literature have reported the antibacterial activity of ZnO NPs and ZnO/CS core–shell nanostructures. For example, Al-Abboodi et al. performed a zone inhibition test and reported that ZnO/CS nanostructure exhibited 42 mm zone inhibition at 20mL/0.05 wt% concentration against *S. aureus* (Al-Abboodi et al. 2020). Li et al. (2010) reported that the inhibition zone diameter increased against *S. aureus* with an increased content of ZnO NPs in the ZnO/CS nanostructure. The antibacterial activity of Bis-GMA/TEGDMA dental composites was slightly observed against *S. aureus*, consistent with the findings of De Mori et al. (2019). However, when DFC6, which contains ZnO/CS nanostructure, was introduced to the Bis-GMA/TEGDMA-Si/PMMA dental composite, the antibacterial effect against the *S. aureus* strain increased from 56 to 95%. The incorporation of ZnO/CS core–shell nanostructure significantly enhanced the antibacterial properties of the dental composite, as reported in studies by Yusof et al. (2019), Javed et al. (2020), and Aykaç and Akkaş (2022). Overall, the results demonstrate the antibacterial potential of Si-based NPs, ZnO NPs, and their respective core–shell nanostructures, as well as the improvement in antibacterial activity when incorporated into dental composites.

Conclusion

In conclusion, the Si/PMMA core–shell nanostructure and ZnO/CS nanostructures were successfully synthesized and characterized. These nanostructures were incorporated into Bis-GMA/TEGDMA (50%/50%) dental composites at different wt% to produce novel inorganic DFC. The mechanical properties of the composite, including flexural strength and flexural modulus, were evaluated using three-point bending tests. Additionally, the antibacterial activity of the composites against *S. aureus* was assessed using colony-forming unit assays. The results of the three-point bending tests showed that DFC6, which contained 0.1% Si/PMMA and 0.5% ZnO/CS nanostructures, exhibited a significant improvement in both flexural strength (46%) and flexural modulus (56%) compared to pristine Bis-GMA/TEGDMA. This suggests that the incorporation

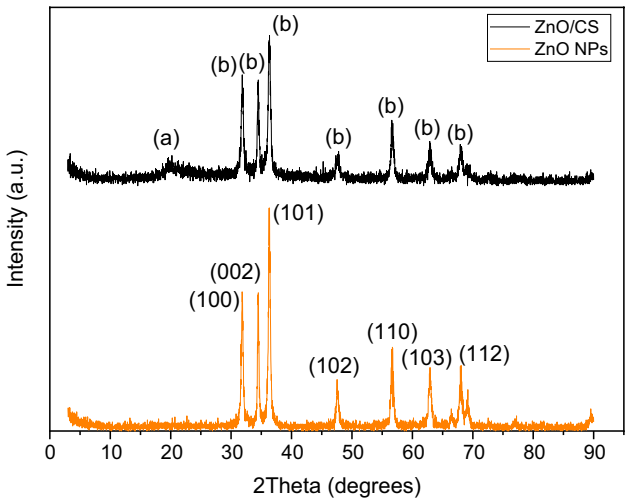

Fig. 7 XRD spectra of ZnO NPs and ZnO/CS core–shell nanostructure

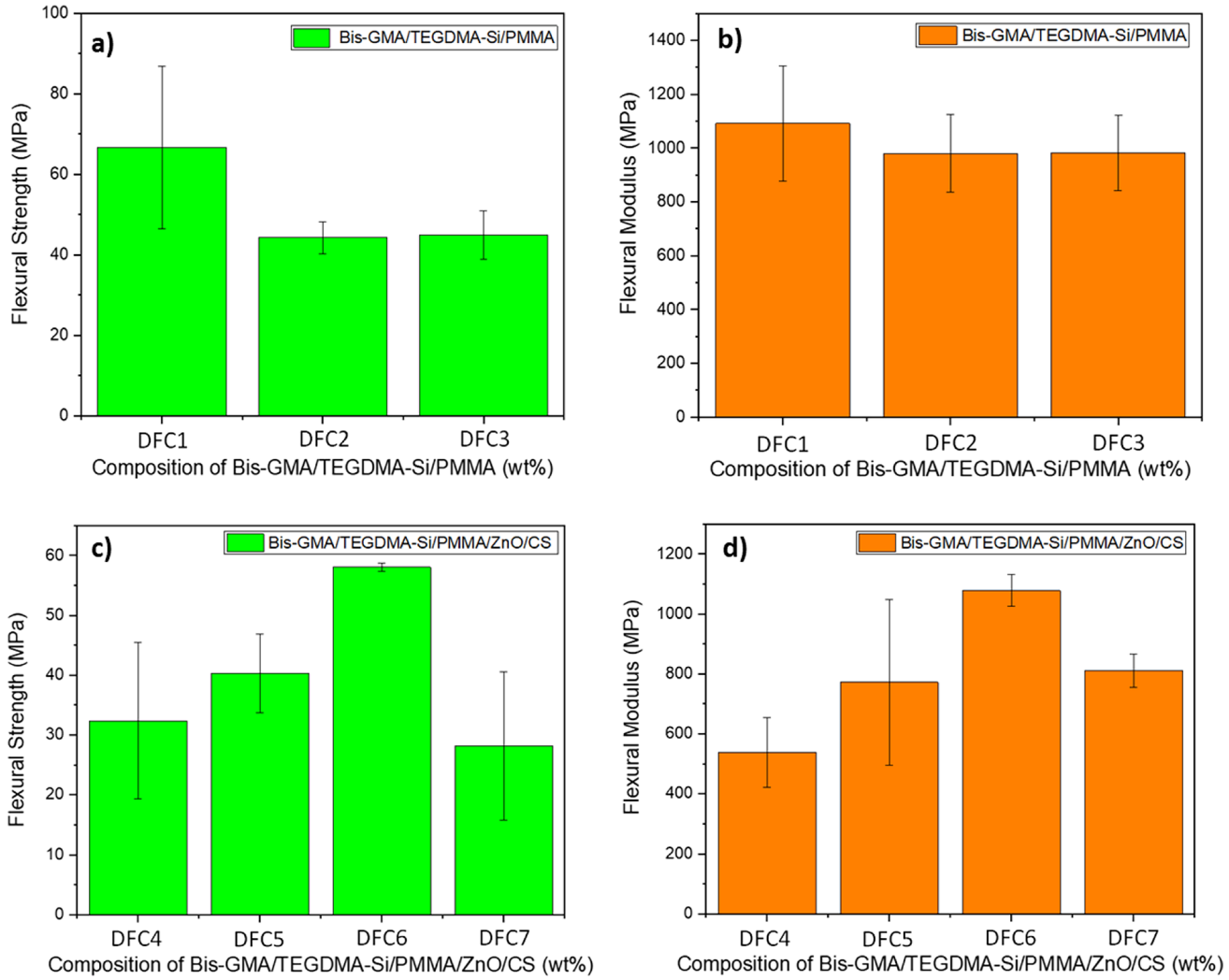

Fig. 8 **a** flexural strength of DFC1, DFC2, and DFC3, **b** flexural modulus of DFC1, DFC2, and DFC3, **c** flexural strength of DFC4, DFC5, DFC6, and DFC7, and **d** flexural modulus of DFC4, DFC5, DFC6, and DFC7

of Si/PMMA and ZnO/CS nanostructures can enhance the mechanical properties of dental composites, potentially reducing issues such as chewing-induced fractures and the need for frequent filler renewal. Furthermore, DFC6 demonstrated the highest antibacterial effect among the tested composites, with a 95% reduction in bacterial colony formation against *S. aureus* strain. The development of these new generation DFC holds promise for improving dental restorative materials in clinical applications.

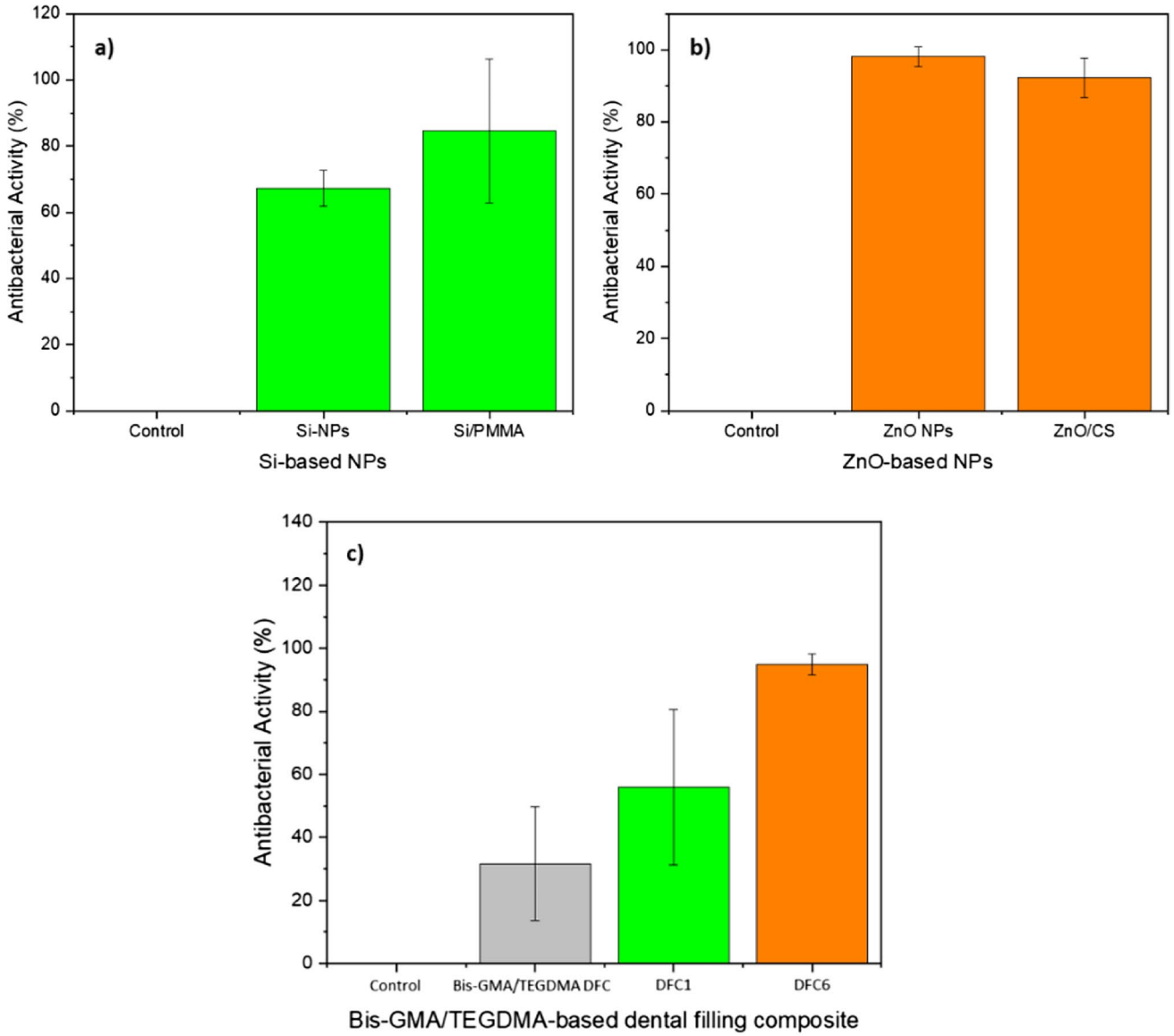

Fig. 9 In vitro antibacterial activity of **a** Si-NPs, Si/PMMA core–shell nanostructure, **b** ZnO NPs, ZnO/CS core–shell nanostructure, and **c** Bis-GMA/TEGDMA DFC, DFC1, and DFC6 against *S. aureus* strain

Supplementary Information The online version contains supplementary material available at https://doi.org/10.1007/s11696-023-02989-9.

Acknowledgements This work was supported by İzmir Katip Çelebi University Scientific Research Council (IKCU-BAP). The authors would like to thank the IKCU-BAP for the financial support via 2021-ÖDL-FEBE-0002 project number.

Author contributions All authors have reviewed and agreed to the published version of the manuscript. IO contributed to conceptualization, methodology, validation, formal analysis, investigation, writing—original draft, and writing—review and editing. AA contributed to conceptualization, methodology, investigation, validation, formal analysis, supervision, resources, review and editing, and funding acquisition.

Data availability The data that support the findings of this study are available upon reasonable request from the authors.

Declarations

Conflict of interest On behalf of all authors, the corresponding author states that there is no conflict of interest.

References

Agnihotri S, Pathak R, Jha D et al (2015) Synthesis and antimicrobial activity of aminoglycoside-conjugated silica nanoparticles against clinical and resistant bacteria. New J Chem 39:6746–6755

Ahmed N, Majid A, Khan MA et al (2018) Synthesis and characterization of Zn/ZnO microspheres on indented sites of silicon substrate. Mater Sci 36:501–508

Al-Abboodi SMT, Yahya AN, Almussawy TA (2020) Preparation and characterization of chitosan/{ZnO}/Ag nanocomposites as antibacterial hydrogel for wound dressing. IOP Conf Ser Mater Sci Eng 978:12040

Al-Shamahy H, Al-labani M (2020) Prevalence of staphylococcus aureus ın dental ınfectıons and the occurrence of MRSA ın ısolates. Univ J Pharm Res 5(2):23–7

Alzraikat H, Burrow M, Maghaireh G, Taha N (2018) Nanofilled resin composite properties and clinical performance: a review. Oper Dent 43:E173–E190

Aykaç A, Akkaş EÖ (2022) Synthesis, characterization, and antibacterial properties of ZnO nanostructures functionalized flexible carbon fibers. Recent Pat Nanotechnol 17(2):119–130

Buşilă M, Muşat V, Textor T, Mahltig B (2015) Synthesis and characterization of antimicrobial textile finishing based on Ag:ZnO nanoparticles/chitosan biocomposites. RSC Adv 5:21562–21571

Canché-Escamilla G, Duarte-Aranda S, Toledano M (2014) Synthesis and characterization of hybrid silica/PMMA nanoparticles and their use as filler in dental composites. Mater Sci Eng C 42:161–167

Cetin AR, Unlu N, Cobanoglu N (2013) A five-year clinical evaluation of direct nanofilled and indirect composite resin restorations in posterior teeth. Oper Dent 38:E31–E41

Chang Q-Q, Cui Y-W, Zhang H-H et al (2019) C-doped ZnO decorated with Au nanoparticles constructed from the metal–organic framework ZIF-8 for photodegradation of organic dyes. RSC Adv 9:12689–12695

Chen Q, Zhao Y, Wu W et al (2012) Fabrication and evaluation of Bis-GMA/TEGDMA dental resins/composites containing halloysite nanotubes. Dent Mater 28:1071–1079

Dananjaya SHS, Kumar RS, Yang M et al (2018) Synthesis, characterization of ZnO-chitosan nanocomposites and evaluation of its antifungal activity against pathogenic Candida albicans. Int J Biol Macromol 108:1281–1288

De Mori A, Di Gregorio E, Kao AP et al (2019) Antibacterial PMMA composite cements with tunable thermal and mechanical properties. ACS Omega 4:19664–19675

El-Banna A, Sherief D, Fawzy AS (2019) 7 - Resin-based dental composites for tooth filling. In: Khurshid Z, Najeeb S, Zafar MS (eds) Sefat FBT-ADB. Woodhead Publishing, New Delhi, pp 127–173

Elizalde-Peña EA, Flores-Ramirez N, Luna-Barcenas G et al (2007) Synthesis and characterization of chitosan-g-glycidyl methacrylate with methyl methacrylate. Eur Polym J 43:3963–3969

Gajewski VES, Pfeifer CS, Fróes-Salgado NRG et al (2012) Monomers used in resin composites: degree of conversion, mechanical properties and water sorption/solubility. Braz Dent J 23:508–514

Gnanasangeetha D, Saralathambavani D (2013) One pot synthesis of zinc oxide nanoparticles via chemical and green method. Res J Mater Sci 1:1–8

Haldorai Y, Shim J-J (2013) Chitosan-zinc oxide hybrid composite for enhanced dye degradation and antibacterial activity. Compos Interfaces 20:365–377

Harb SV, dos Santos FC, Pulcinelli SH et al (2016) Protective coatings based on PMMA–silica nanocomposites reinforced with carbon nanotubes. In: Berber MR, Hafez IH (eds) Carbon nanotubes. IntechOpen, Rijeka

Javed R, Rais F, Fatima H et al (2020) Chitosan encapsulated ZnO nanocomposites: fabrication, characterization, and functionalization of bio-dental approaches. Mater Sci Eng C 116:111184

Kaptan Usul S, Aslan A, Lüleci HB et al (2022) Investigation of antimicrobial and mechanical effects of functional nanoparticles in novel dental resin composites. J Dent 123:104180

Karabela MM, Sideridou ID (2011) Synthesis and study of properties of dental resin composites with different nanosilica particles size. Dent Mater 27:825–835

Khademi M, Wang W, Reitinger W, Barz DP (2017) The Zeta potential of poly PMMA in contact with aqueous electrolyte–surfactant solutions. Langmuir 33(40):10473–10482

Kim HC, Noh SM, Park SK (2013) Synthesis and characterization of nanosilica ball-PMMA hybrid composites. J Appl Polym Sci 127:1653–1658

Kumar S, Koh J (2012) Physiochemical, optical and biological activity of chitosan-chromone derivative for biomedical applications. Int J Mol Sci 13:6102–6116

Kundie F, Azhari CH, Muchtar A, Ahmad ZA (2018) Effects of filler size on the mechanical properties of polymer-filled dental composites: a review of recent developments. J Phys Sci 29:141–165

Li L-H, Deng J-C, Deng H-R et al (2010) Synthesis and characterization of chitosan/ZnO nanoparticle composite membranes. Carbohydr Res 345:994–998

Masud RA, Islam MS, Haque P et al (2020) Preparation of novel chitosan/poly (ethylene glycol)/ZnO bionanocomposite for wound healing application: effect of gentamicin loading. Materialia 12:100785

McCormack MG, Smith AJ, Akram AN et al (2015) Staphylococcus aureus and the oral cavity: an overlooked source of carriage and infection? Am J Infect Control 43:35–37

Nguyen NT, Nguyen NT, Nguyen VA (2020) In situ synthesis and characterization of ZnO/chitosan nanocomposite as an adsorbent for removal of congo red from aqueous solution. Adv Polym Technol 2020:3892694

Petrizza L, Collot M, Richert L et al (2016) Dye-doped silica nanoparticle probes for fluorescence lifetime imaging of reductive environments in living cells. RSC Adv 6:104164–104172

Salehi R, Mahmoodi NM, Bahrami H, Khorramfar S (2010) Novel biocompatible composite (Chitosan-zinc oxide nanoparticle): Preparation, characterization and dye adsorption properties. Colloids Surf B Biointerfaces 80:86–93

Şen Karaman D, Gulin-Sarfraz T, Hedström G et al (2014) Rational evaluation of the utilization of PEG-PEI copolymers for the facilitation of silica nanoparticulate systems in biomedical applications. J Colloid Interface Sci 418:300–310

Sodagar A, Khalil S, Kassaee MZ et al (2016) Antimicrobial properties of poly (methyl methacrylate) acrylic resins incorporated with silicon dioxide and titanium dioxide nanoparticles on cariogenic bacteria. J Orthod Sci 5:7–13

Song W, Ge S (2019) Application of antimicrobial nanoparticles in dentistry. Molecules 24:1033

Sundeep D, Vijaya Kumar T, Rao PSS et al (2017) Green synthesis and characterization of Ag nanoparticles from Mangifera indica leaves for dental restoration and antibacterial applications. Prog Biomater 6:57–66

Swain SK, Dey RK, Islam M et al (2009) Removal of fluoride from aqueous solution using aluminum-impregnated chitosan biopolymer. Sep Sci Technol 44:2096–2116

Taslı H, Akbıyık A, Topaloğlu N et al (2018) Photodynamic antimicrobial activity of new porphyrin derivatives against methicillin resistant Staphylococcus aureus. J Microbiol 56:828–837

Vega-Jiménez AL, Almaguer-Flores A, Flores-Castañeda M et al (2017) Bismuth subsalicylate nanoparticles with anaerobic

antibacterial activity for dental applications. Nanotechnology 28:435101
Wang H, Ren D (2017) Controlling Streptococcus mutans and Staphylococcus aureus biofilms with direct current and chlorhexidine. AMB Express 7:204
Wilson KS, Antonucci JM (2006) Interphase structure-property relationships in thermoset dimethacrylate nanocomposites. Dent Mater 22:995–1001
Yang Y, Dan Y (2003) Preparation of PMMA/SiO_2 composite particles via emulsion polymerization. Colloid Polym Sci 281:794–799
Yang Y, Xu Z, Guo Y et al (2021) Novel core–shell CHX/ACP nanoparticles effectively improve the mechanical, antibacterial and remineralized properties of the dental resin composite. Dent Mater 37:636–647
Yusof NAA, Zain NM, Pauzi N (2019) Synthesis of ZnO nanoparticles with chitosan as stabilizing agent and their antibacterial properties against Gram-positive and Gram-negative bacteria. Int J Biol Macromol 124:1132–1136
Zaharia A, Muşat V, Pleşcan Ghisman V, Baroiu N (2016) Antimicrobial hybrid biocompatible materials based on acrylic copolymers modified with (Ag)ZnO/chitosan composite nanoparticles. Eur Polym J 84:550–564
Zhang H, Li C, Guo J et al (2012) In situ synthesis of poly(methyl methacrylate)/SiO2 hybrid nanocomposites via “grafting onto” strategy based on UV ırradiation in the presence of ıron aqueous solution. J Nanomater 2012:1–9
Zhang F, Lan J, Yang Y et al (2013) Adsorption behavior and mechanism of methyl blue on zinc oxide nanoparticles. J Nanopart Res 15:1–10
Zhao D, Yu S, Sun B et al (2018) Biomedical applications of chitosan and its derivative nanoparticles. Polymers 10:462

Authors and Affiliations

Izel Ok[1] · Ahmet Aykac[1,2]

✉ Ahmet Aykac
ahmet.aykac@ikcu.edu.tr

[1] Department of Nanoscience and Nanotechnology, Izmir Katip Celebi University, 35620 Izmir, Turkey

[2] Department of Engineering Sciences, Izmir Katip Celebi University, 35620 Izmir, Turkey